Experiments in Fluids (2021) 62:240
https://doi.org/10.1007/s00348-021-03337-x

RESEARCH ARTICLE

Structure and mixing of a meandering turbulent chemical plume: concentration and velocity fields

David L. Young[1,2] · Ann I. Larsson[1,3] · Donald R. Webster[1]

Received: 8 July 2021 / Revised: 21 September 2021 / Accepted: 14 October 2021

Abstract
This study presents simultaneous particle image velocimetry (PIV) and laser-induced fluorescence (LIF) measurements of a phase-locked meandering chemical plume, the motion of which is forced by the periodic oscillation of a diverting plate. The plume evolves in a turbulent boundary layer in a moderate-Reynolds-number open channel flow. For the meandering plume, the centerline phase-averaged concentration decreases more rapidly with downstream distance and the plume width increases more rapidly with downstream distance (as x^1) compared to the straight plume (as $x^{3/4}$). Furthermore, the concentration fields and transverse profiles are asymmetric about the plume centerline in the meandering plume. Nevertheless, the transverse profiles can be modeled by a Gaussian shape in a segmented manner. The velocity fields indicate that the large-scale alternating-sign vortices induced by the diverting plate are the dominant feature of the flow. The vortices induce the plume to meander and govern the spatial distribution of the phase-averaged concentration. The induced fluid motion by the vortices also helps in explaining the increased mixing and dilution of the concentration field. Further, a phenomenological model of chemical filament transport by the vortical motion explains local peaks in the phase-averaged concentration along the plume centerline.

Graphical abstract

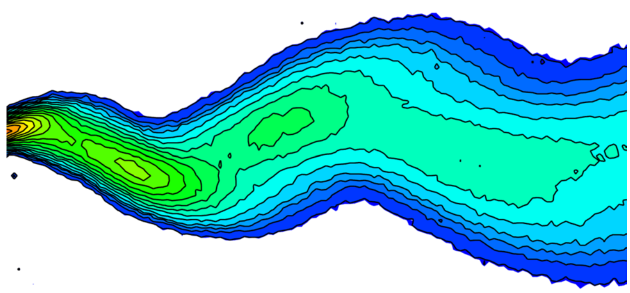

1 Introduction

Turbulent chemical plumes are of substantial importance in a number of atmospheric and aquatic contexts, including point sources of pollution and hazardous substances, design of ocean and river outfalls, control of water and air quality, airborne virus transmission, and odorant tracking strategies by biological organisms. Much is known regarding the dynamics of straight plumes in turbulent boundary layers (e.g., Bara et al. 1992; Crimaldi et al. 2002; Webster et al. 2003; Rahman and Webster 2005; Crimaldi and Koseff 2006) and uniformly sheared flows (Vanderwel and

✉ Donald R. Webster
dwebster@ce.gatech.edu

David L. Young
david.l.young@usace.army.mil

1 School of Civil and Environmental Engineering, Georgia Institute of Technology, 790 Atlantic Drive, Atlanta, GA 30332, USA

2 US Army Corps of Engineers, 1261 Duck Road, Kitty Hawk, NC 27949, USA

3 Department of Marine Sciences, Tjärnö Marine Laboratory, University of Gothenburg, 45296 Strömstad, Sweden

Published online: 09 November 2021

Tavoularis 2014a,2014b). The work on uniformly sheared flows, in particular, elucidates the influence of the turbulent vortical structures on mixing. However, many naturally occurring plumes meander, which is defined as large-scale movement of the plume centerline. This phenomenon is most commonly observed in atmospheric plumes (Thomson et al. 1977; Kristensen et al. 1981; DeFelice et al. 2000), but also occurs in flows that naturally oscillate, such as the wake flow past a cylinder (i.e., the von Kármán vortex street) or other bluff body flows (e.g., islands in coastal seas or estuaries Wolanski et al. 1984; Ingram and Chu 1987; Cramp et al. 1991; Stacey et al. 2000; Fong and Stacey 2003).

Plumes released in an atmospheric boundary layer are perhaps the most-studied case of meandering plumes. Atmospheric plume meander is commonly observed in low-wind speed conditions, where large-scale horizontal oscillations in the wind velocity become dominant in governing the plume motion (Etling 1990; Anfossi et al. 2005; Oettl et al. 2005). In meandering plumes, concentration fluctuations are caused not only by turbulence, but also by the large-scale motion of the plume centerline (Hanna 1984; Sykes 1984; Wilson et al. 1985; Liao and Cowen 2010). Studies that attempt to describe meandering plumes often struggle to separate turbulent fluctuations from fluctuations associated with the movement of the plume centerline (Yee et al. 1994; Luhar et al. 2000; Reynolds 2000; Yee and Wilson 2000; Franzese 2003; Mortarini et al. 2009), due to ensembling of point measurements, often in the field, where phase-locking is impossible. It is also common to sample with a mobile sensor performing a transect through the meandering plume structure, which adds a confounding temporal uncertainty to the measurements (e.g., Csanady 1973; Stacey et al. 2000; Fong and Stacey 2003).

One of the earliest analytical models of meandering plumes is that of Gifford (1959) and the assumptions made in developing it are a natural starting point for many later studies (e.g., Csanady 1973; Sawford and Stapountzis 1986; Hanna 1986; Ride 1988; Bara et al. 1992; Talluru et al. 2018). In the Gifford (1959) plume model, the plume disperses about an instantaneous centerline located some distance (D_y) away from the center axis. The key conceptual assumption in the Gifford (1959) model is that the meander of the plume is due to large-scale eddies (those larger than the plume width) that move the plume centerline but do not contribute to the mixing. In other words, there is a separation of scales between the flow structures inducing the meander and the turbulent diffusion (or dispersion), and these can be considered as independent processes. This is analogous to turbulent mixing phenomenological models, in which eddies larger than the scalar "patch" merely advect the patch and only eddies of the same size or smaller than the patch contribute to mixing. In this model, transverse turbulent diffusion is quantified by the plume width as measured by the standard deviation of the transverse concentration profile (σ_y). The Gifford (1959) model also entirely neglects longitudinal turbulent diffusion. Under these restrictions, Gifford (1959) proposed a model that is identical to the solution of the turbulent advection–diffusion equation for a straight plume, with the addition that the plume centerline is located some displaced position away from the center axis. As with the straight plume solution, the Gifford (1959) plume model predicts transverse profiles with a Gaussian mean concentration distribution about the instantaneous plume centerline.

Quantifying the precise location of the instantaneous plume centerline presents significant challenges for modeling atmospheric plumes. Several recent studies (e.g., Nironi et al. 2015; Marro et al. 2015) propose generating probability density functions (PDFs) of the concentration at a given location downwind by taking the convolution of the PDF of the location of the plume centerline with the PDF of the concentration in a frame of reference along the instantaneous plume centerline. The PDF of the location of the plume centerline is generally assumed to be a product of the transverse and vertical PDFs of the plume centreline—which is an admitted assumption of convenience rather than theoretical rigor (Marro et al. 2015). It is important to note that for this PDF convolution approach to be applicable, it must be assumed that the location of the plume centerline and the concentration in a frame of reference along the plume centerline are independent random variables. That is to say that the assumptions of the Gifford (1959) approach regarding the independence of the plume meander and the relative turbulent diffusion about the instantaneous centerline must be valid.

Although atmospheric plumes are perhaps the most studied instance of plume meandering, there are other situations in which scalar plumes meander. Consider the von Kármán vortex street formed in the wake of bluff bodies such as a circular cylinder. von Kármán vortex streets or similar periodic structures can be observed in the environment when the wake structure is largely two-dimensional. Predominantly two-dimensional wake structure can be the result of density stratification in the ambient fluid inhibiting vertical mixing (Thomson et al. 1977) or can be observed in very shallow flows with large horizontal extent (von Carmer et al. 2009). Quasi-periodic vortex shedding has been observed in a variety of flows, including: shallow two-dimensional wake flows past islands in coastal seas and estuaries (Wolanski et al. 1984; Ingram and Chu 1987; Cramp et al. 1991), shallow two-dimensional wake flows past anthropogenic obstacles (e.g., Van Dyke 1982), and in the wake structure behind mountain peaks under strong density stratification (Thomson et al. 1977; DeFelice et al. 2000).

Given that the large-scale oscillations of the wake structure behind bluff bodies are observed for a wide range of Reynolds numbers, it is reasonable to expect the plume of any scalar quantity released in the wake to meander. Indeed, studies of concentration fields in the wake of flows past bluff bodies have observed large-scale periodic plume meandering (Bo et al. 2003; von Carmer et al. 2009). That the wake structure of flows past bluff bodies frequently exhibits a dominant periodicity offers hope that the plume centerline may be defined by an oscillatory function. This would make the problem of plume meandering more tractable than the complex PDF convolution approach common in the atmospheric plume literature.

This study examines the mixing of a chemical scalar in a meandering plume by phase-locking the plume to separate the fluctuations due to the plume meander from the turbulent velocity and concentration fluctuations. Simultaneous laser-induced fluorescence (LIF) and particle image velocimetry (PIV) data of the phase-locked meandering plume structure facilitate direct comparison of the structure of the phase-locked concentration field for the meandering plume to prior straight plume studies (e.g., Crimaldi et al. 2002; Rahman and Webster 2005; Crimaldi and Koseff 2006). This study therefore provides an unprecedented spatial perspective to turbulent meandering plumes, which most notably have been studied with point measurements. The field studies referenced above also lacked the advantage of phase-locked measurements, which facilitate insight into the interaction between turbulent mixing and the large-scale meandering. The objective of this study is to quantify the large-scale meandering motion and provide fundamental insight to the phase-averaged velocity and concentration fields. In Young et al. (2022), the turbulent mixing characteristics are examined in detail and the effectiveness of the eddy diffusivity model is evaluated.

2 Materials and methods

To study the turbulent transport of a passive scalar in a meandering turbulent plume, simultaneous particle image velocimetry (PIV) and laser-induced fluorescence (LIF) measurements were performed to quantify the velocity and concentration fields, respectively (e.g., Law and Wang 2000; Webster et al. 2001). Data were also collected (LIF only) for a straight plume in the same flume for comparison with the meandering plume results.

2.1 Experimental design

All experiments were performed in a 1.07 m wide by 24.4 m long rectangular cross-section tilting flume (Fig. 1). The flume head box was filled with water at 22 °C from an underground sump by a submerged pump. The water was dechlorinated prior to the experiments and a stilling device in the flume head box minimized the turbulence intensity of the flow entering the flume. Uniform depth ($H = 200 \pm 0.1$ mm) flow was created for at least 12 m upstream of the test section by adjusting the tailgate position and bed slope. Tracy and Lester (1961) and Rahman and Webster (2005) confirmed that a fully developed turbulent boundary layer is generated in the test section under these conditions. The mean velocity profile in the bottom boundary layer matches the law-of-the-wall very well with $u^* = 3.08$ mm/s (Fig. 2a) as previously reported in Rahman and Webster (2005). Further, the streamwise Reynolds normal stress profile in the turbulent boundary layer is consistent with previous experiments and simulations (Fig. 2b). The sidewall of the flume in the vicinity of the test section is glass for direct optical access.

A PVC plastic diverting plate (25.3 cm tall, 10.1 cm long, and 2.54 cm thick) suspended in the flume induced the plume meandering. The diverting plate was designed such that the flow characteristics in the wake were analogous

Fig. 1 Schematic layout of the experiment from an overhead perspective

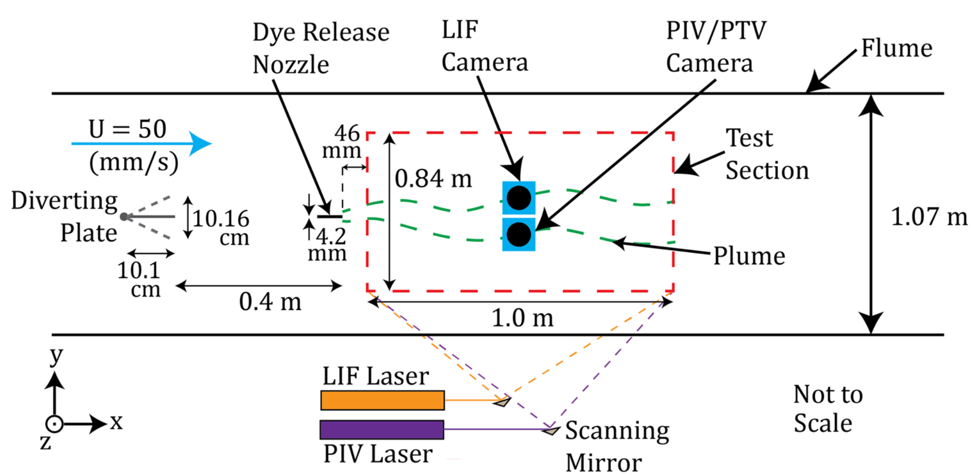

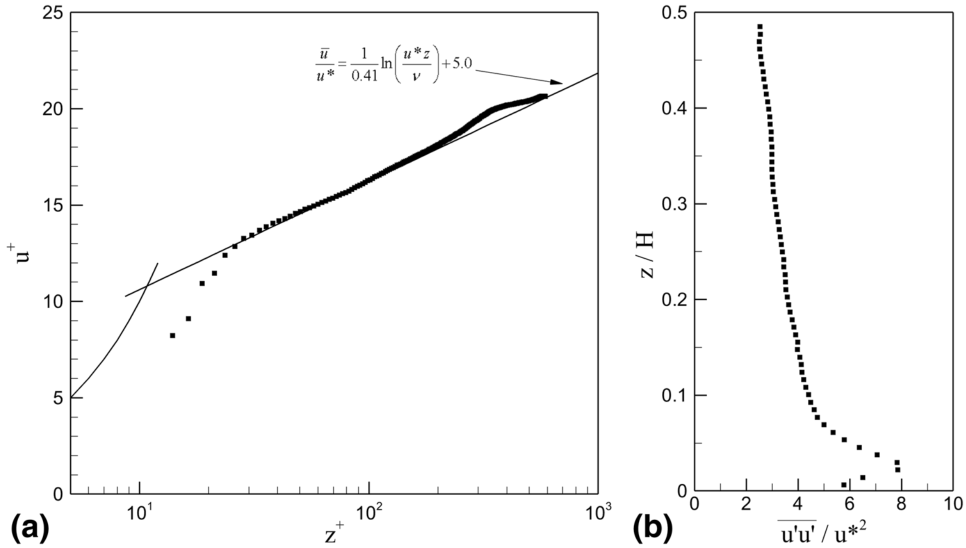

Fig. 2 **a** Normalized mean streamwise velocity profile, and **b** normalized streamwise Reynolds normal stress profile for the bed boundary layer flow. The wall shear velocity is $u^* = 3.08$ mm/s

to the wake downstream of a 10.1 cm diameter circular cylinder for the same water depth and free-stream velocity ($H = 200$ mm and $U = 50$ mm/s, respectively, $Re_H = 10{,}000$, $Re_{cylinder} = 5000$). The advantage of a meandering plume generated by a periodically oscillating plate is that it facilitated data-acquisition triggering (via a mechanical trigger attached to the diverting plate apparatus) to collect data at specific phases in the plate motion. The base of the plate was positioned less than 1 mm above the flume bed and the top of the plate extended above the free surface. A vertical rod through the upstream edge of the plate provided a fixed pivot location. A DC motor attached to the diverting plate via a disk and linkage mechanism forced the motion of the downstream edge of the plate. The period of the plate oscillation (T) was 9.5 s, and the amplitude of the transverse displacement of the downstream edge of the plate was 5.08 cm. The resulting Strouhal number is St = 0.21.

Figure 1 shows a schematic representation of the experiment configuration from an overhead perspective. The passive scalar (florescent dye) was released 400 mm downstream of the diverting plate and 46 mm upstream of the test section. The neutrally buoyant dye was released iso-kinetically through a 4.2 mm diameter nozzle, located 20 mm above the flume bed. The 1.2 cm long nozzle fairing was streamlined to minimize the flow disturbance (Webster et al. 2003; Rahman and Webster 2005). The origin of the x and y axes is at the nozzle tip, and $z = 0$ at the flume bed.

2.2 Laser and camera optics

Illumination for the LIF measurements was provided by a 10 W Argon-ion laser (Coherent Innova 90, Coherent Inc., Santa Clara, CA) with a wavelength of 514 nm. The laser was operated in open-aperture mode and passed through two 4 m focal length lenses, resulting in a beam diameter of 1 mm in the center of the plume. The illumination for the PIV measurements was provided by a 4.6 W Krypton-ion laser (Coherent Innova Sabre, Coherent Inc., Santa Clara, CA) with a wavelength of 647.1 nm. The beam did not pass through any focal lenses, resulting in a beam diameter at the plume center of 1.5 mm.

The laser beams were swept in the streamwise direction via scanning mirrors controlled with a National Instruments multi-purpose I/O module programmed in LabView (National Instruments Corporation, Austin, TX). The resulting horizontal light sheets were formed 20 mm above the flume bed (the same height as the florescent dye release). The LIF and PIV images were captured with two side-by-side digital cameras (sCMOS pco.edge, PCO AG, Kelheim, Germany) operating in global shutter mode and mounted 1.5 m above the flume bed at the test section. Each camera was equipped with a 24 mm Nikon lens (Nikon, Tokyo, Japan) at a f-stop of f/2.0. The LIF camera was further equipped with a bandpass filter (Omega Optical Inc., Brattleboro, Vermont) which passed light with a wavelength of 555 ± 15 nm (i.e., in the band of the wavelength emitted by the fluorescent dye). An optical high pass filter (Tiffen Orange 21) with cutoff around 560 nm was placed on the PIV camera to eliminate the laser light from the Argon-ion laser. The cameras provide 16-bit 2560 × 2160 pixel images that span 1000 mm of the flume in the streamwise direction and 840 mm in the transverse direction. A 19 mm thick acrylic sheet was suspended just above the water surface (wetting the bottom surface of the sheet only) during the experiment to prevent optical distortion from the free surface.

2.3 Timing system and laser scanning

The PIV and LIF images were acquired simultaneously for four phases ($\varphi = 0°$, $\varphi = 90°$, $\varphi = 150°$, and $\varphi = 240°$) in the diverting plate motion. Phase $\varphi = 0°$ is defined as the orientation of maximum transverse displacement of the diverting plate position. For the LIF dataset, 6706 images were acquired for each phase, with a 9.5 s delay between successive images of a given phase. Similarly, for the PIV dataset, 6706 image pairs were acquired for each phase. Thus, the total experiment time is approximately 17.5 h.

To synchronize to the diverting plate motion, a mechanical push switch was installed on the diverting plate to trigger the image acquisition sequence. The trigger signal from the push switch externally triggered a series of two precision pulse generators (Model 500D, Berkeley Nucleonics Corporation, San Rafael, CA) that generated the delayed signals to the cameras to collect images for the four phases and to the National Instruments multi-purpose I/O module that controlled the laser sweeps. First, the PIV laser was swept to acquire the first image of the PIV image pair, second the LIF laser was swept to acquire the LIF image, and finally the PIV laser was swept again to acquire the second image of the PIV image pair. The timing of the LIF laser sweep was at the mid-time-point between the two PIV laser sweeps, which were separated by 55 ms. The laser sweep durations were 15 ms for the PIV laser and 38 ms for the LIF laser. The PIV laser sweep rate was uniform in order to yield uniformly illuminated particles throughout the imaging region. The LIF laser sweep rate was non-uniform—configured such that the light intensity increased with distance away from the plume source. The non-uniform LIF laser sweep was governed by the power law control voltage signal described in Webster et al. (2003), $E = E_0 + \left(E_1 + E_0\right)\left(\frac{t}{\tau}\right)^{\frac{1}{n+1}}$, where E_0 and E_1 are the start and end voltages, respectively, and τ is the period of the sweep. The value of $n = 1$ produced the most uniform raw LIF images for both the meandering plume and straight plume cases, thereby taking advantage of the camera's dynamic range over the entire pixel array.

2.4 Particle image velocimetry

To acquire the PIV images, the water was seeded with a solution (0.9 g/L) of 20 µm diameter polyamide particles (Orgasol 2002 D NAT 1, Arkema Inc., King of Prussia, PA). The seeding solution was pumped through a copper diffuser with eight 1.6 mm diameter holes spanning the width of the flume at 38 L/hr. The diffuser was located 30 mm above the flume bed, 9 m upstream of the test section. This resulted in a well-mixed particle distribution with an average particle concentration in the flume of 0.9 mg/L. Images from the PIV camera were captured using Camware (PCO AG, Kelheim, Germany) on the fast image sensor readout speed (286 MHz) to avoid frame dropping, resulting in 12-bit images rather than the full camera resolution (16-bit). The images were imported into the DaVis software (LaVision GmbH, Göttingen, Germany) to acquire the velocity vectors using the PIV algorithm packages. The interrogation window for the PIV analysis was 16×16 pixels. The uncertainty for the velocity measurements was estimated to be $\pm 1\%$ based on consideration of the cross-correlation image analysis. Spurious vectors accounted for fewer than 0.5% of the total number of vectors calculated.

2.5 Laser-induced fluorescence

Laser-induced Fluorescence (LIF) was used to acquire the concentration field in the plume. To perform LIF, fluorescent dye was released into the flow through the 4.2 mm diameter nozzle. A light sheet from a laser passes through the flow and causes the dye in the flow to fluoresce (Crimaldi 2008). The intensity of light released by the fluorescent dye is proportional to the concentration under the appropriate conditions. Images of the flow and fluorescing dye are captured by a digital camera, and the amount of light at each pixel is converted to concentration by a LIF calibration function. As the concentration is measured at each pixel, the LIF concentration fields are highly spatially resolved (0.4 mm per pixel in these experiments).

The fluorescent dye used in the current experiments was Rhodamine 6G, which has peak light absorption at 530 nm (near the wavelength of the Argon-ion laser) and peak emission near 560 nm (Arcoumanis et al. 1990). Powdered Rhodamine 6G was mixed with de-ionized water to yield a high-concentration stock solution of dye (200 mg/L). This stock solution was used for LIF calibration and to mix the dye solution that was released into the flume. The meandering plume source concentration was chosen to be 1 mg/L (0.5 mg/L for the straight plume) to make use of the full dynamic range of the LIF camera.

The images from the LIF camera were captured using Camware at a slower image sensor readout speed (95 MHz) resulting in 16-bit images. The images were imported into the DaVis software to calculate the concentration fields using the LIF analysis package. The fluorescent light intensity was corrected to account for the non-uniform sweep rate of the LIF laser using the DaVis laser sheet correction function, which requires images of the laser sheet passing through a uniform low concentration of dye. To achieve this, the imaging region was isolated from the rest of the flume via dams located upstream and downstream of the test section. The test section was filled to a depth of 200 mm with a known volume of water, and Rhodamine 6G fluorescent dye was added to reach a uniform concentration of 5 µm/L in the

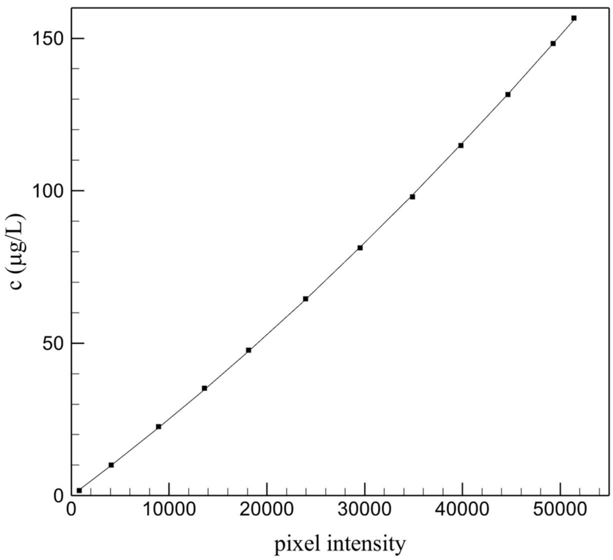

Fig. 3 Camera calibration relationship for the LIF measurements. The line is a 2nd-order polynomial fit function ($R^2 = 0.999$)

test section. Two hundred images of this configuration using the non-uniformly swept LIF laser were used to generate the DaVis laser sheet correction function.

A calibration function describing the relationship between the dye concentration and the emitted light intensity is necessary to ensure accurate scalar concentration results. Therefore, a polyacrylic tank (1200 × 500 × 250 mm) was centrally placed in the test section, and filled with water to a depth of 200 mm. To perform the calibration, Rhodamine 6G was added to the tank to a concentration of 1.7 µm/L and 100 images of this configuration using a uniform sweep of the LIF laser were acquired. This was repeated eleven additional times to yield calibration images for uniform Rhodamine 6G concentrations between 1.7 and 157 µm/L. The relationship between the dye concentration and the emitted light intensity was non-linear (particularly at low dye concentrations), thus a 2nd-order polynomial calibration function was used ($R^2 = 0.999$—Fig. 3). The uncertainty in the instantaneous concentration measurements was estimated to be ± 3% based on several factors including the calibration procedure (see Ferrier et al. 1993 and Webster et al. 2003 for a detailed presentation of applying the LIF measurement technique).

2.6 Camera calibration

To calibrate the image region of the PIV and LIF cameras, images of a 2D calibration panel (a grid of 20 mm dots spaced 80 mm apart) placed in the flume bed were taken by each camera. To create the same optical path as during the data collection, the flume was filled with water and the acrylic sheet was placed on the free surface during camera calibration. The recorded calibration images allowed the recorded PIV and LIF images to be corrected for oblique viewing and distortion, and in addition the images from the two cameras were aligned and indexed. The polynomial 2nd-order calibration function in the DaVis software was used for the camera calibration.

3 Results and discussion

3.1 Instantaneous concentration and velocity

Dye-flow visualization images (Fig. 4) and instantaneous concentration and velocity field figures (Fig. 5) aid substantially in qualitative understanding of meandering plumes. For instance, the large-scale meander of the plume

Fig. 4 Example flow visualization image from an overhead perspective of the meandering plume for phase $\varphi = 0°$. Flow direction is from left to right

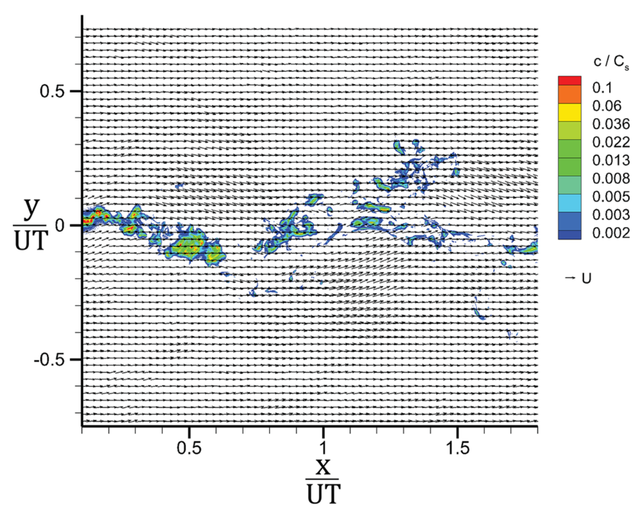

Fig. 5 Example simultaneous velocity (PIV) and concentration fields (LIF) of the meandering plume for phase $\varphi = 0°$. Note the concentration contour levels are logarithmically spaced

centerline is readily visible in Figs. 4 and 5. These figures also highlight the filamentous nature of the instantaneous scalar concentration in turbulent plumes—in Fig. 4 one observes the dye filaments as they are stretched and distorted by turbulent eddies, resulting in the large concentration gradients that make turbulent mixing so effective. This rapid mixing is observed in Fig. 4, as the dye is visibly more dilute to the downstream (right) side of the image. The intermittent and random nature of the turbulent plume is evidenced in the noticeably patchy instantaneous concentration distribution in Fig. 5. Note that the axes of Fig. 5 (and in subsequent figures) have been normalized by the free-stream velocity multiplied by the period of the diverting plate oscillation (UT), which provides a normalizing scale related to the meander.

3.2 Plume centerline

A defining feature of a turbulent plume is the location of the plume centerline. The plume centerline is defined as the location of maximum average (in this case phase-averaged) concentration at each position downstream of the plume source. The centerline locations for the four phases of the meandering plume, as well as the straight comparison plume, based on this criterion are shown in Fig. 6a. The centerline locations presented in Fig. 6a have been smoothed with a weighted linear least-squares fit to a second-order polynomial. Figure 6a shows that the amplitude of the plume meander is initially small, then rapidly increases to a maximum between $x/UT = 0.5$ and $x/UT = 1.5$. Upon reaching the peak, the meander amplitude slowly decreases with increasing downstream distance. The wavelength of the plume centerline meander is initially $x/UT = 0.84$ for all four phases of the meandering plume and appears to increase with downstream distance. Note that the centerline of the straight plume also exhibits small-scale offsets from the center axis, hence the distinguishing characteristic between the "straight" and "meandering" plumes is the magnitude of the offset of the centerline from $y = 0$.

Figure 6b shows the phase-averaged concentration along the plume centerline. As expected, the concentration is greatest upstream and rapidly decreases with downstream distance. The centerline phase-averaged concentration decreases faster for the meandering plume relative to the straight plume, which indicates greater mixing and dilution in the meandering plume. Whereas the concentration decreases monotonically for the straight plume, local minimums and maximums are observed in the phase-averaged concentration for each of the four phases of the meandering plume.

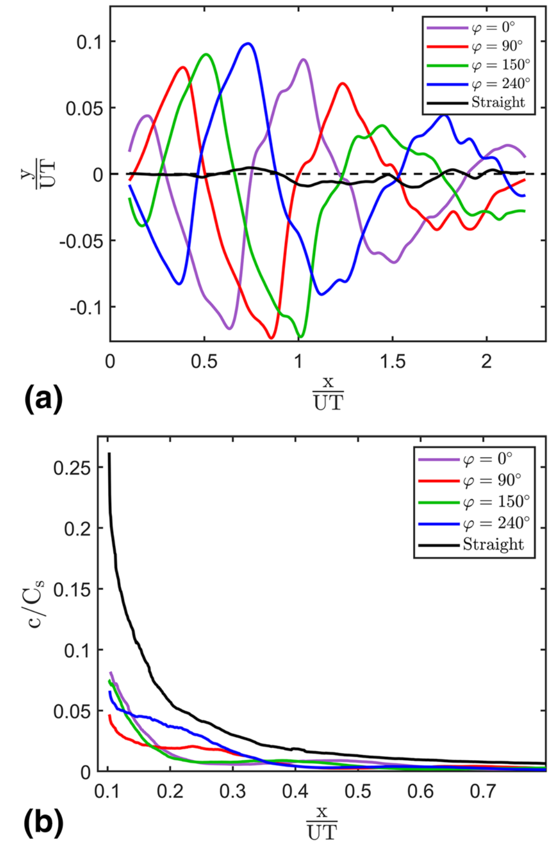

Fig. 6 **a** Plume centerline location, and **b** phase-averaged concentration along the centerline for the meandering plume for phases $\varphi = 0°$, $\varphi = 90°$, $\varphi = 150°$, and $\varphi = 240°$ and for the straight plume

3.3 Phase-averaged concentration and concentration fluctuations

The spatial variability in the phase-averaged concentration and the standard deviation of the concentration fluctuations for the meandering plume for phase $\varphi = 0°$ are shown in Fig. 7. Figure 7a clearly reveals the meandering shape of the plume structure with the largest phase-averaged concentration located at the plume centerline location and the phase-averaged concentration decreasing in steep transverse gradients. The local minimums and maximums of the phase-averaged concentration along the plume centerline previously seen in Fig. 6b are also observed as peaks and valleys in the contour plot of Fig. 7a. As discussed in greater detail below, these local minimums and maximums are the result of transport by the large-scale alternating-sign vortices that are periodically shed from the diverting plate and induce the plume meander. While the plot of standard deviation of the concentration fluctuations in Fig. 7b is noisier than the phase-averaged concentration, the general structure is qualitatively similar: the intensity of the concentration fluctuations visually appears co-located with high-values of the

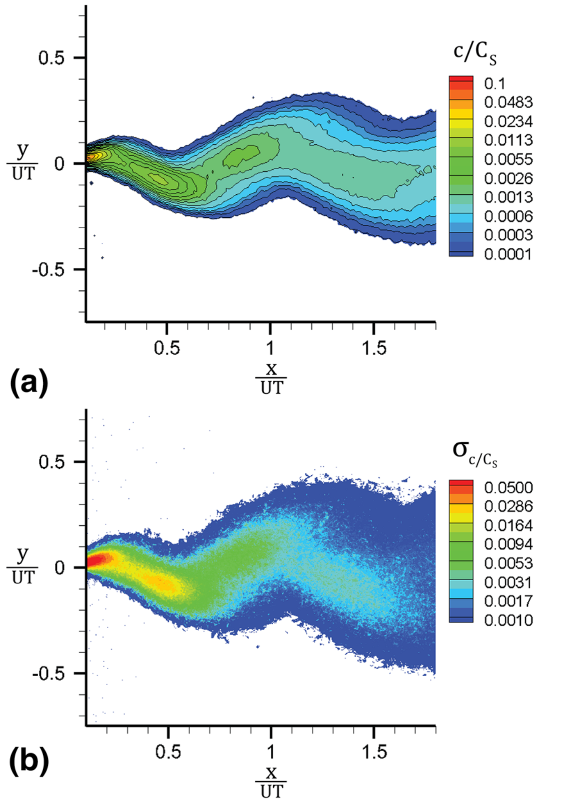

Fig. 7 **a** Phase-averaged concentration field, and **b** standard deviation of the concentration fluctuations (σ_{c/C_s}) of the meandering plume for phase $\varphi = 0°$. Note the contour levels are logarithmically spaced

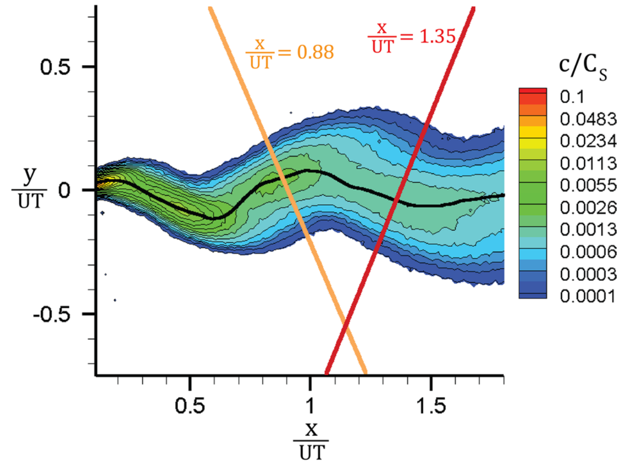

Fig. 8 Sketch of the plume centerline for the meandering plume for phase $\varphi = 0°$, noting two example transects that are perpendicular to the local plume centerline, which define the local y_0 axes

phase-averaged concentration, including the local minimums and maximums. The contour map of the standard deviation of the concentration fluctuations is slightly wider than the corresponding contour map of the phase-averaged concentration, which is consistent with the plume structure in straight plumes in uniformly sheared flows (Vanderwel and Tavoularis 2014a).

3.4 Concentration transects

To extract across-plume profiles, the transects are aligned perpendicularly to the local plume centerline rather than simply in the transverse coordinate direction. As shown in Fig. 8 for phase $\varphi = 0°$, such definition of the transect axes effectively orients the transects perpendicular to the iso-contours of the phase-averaged concentration field. In this orientation, the largest concentration gradient (where the largest turbulent flux would be expected) occurs along the transect axes. Such alignment also has the advantage of facilitating consideration of an eddy diffusivity model of the turbulent mixing as done in the companion paper (Young et al. 2022). In subsequent figures and analysis, the axis direction perpendicular to the local plume centerline is referred to as y_0.

Figure 8 also reveals that the phase-averaged concentration field is asymmetric between the left and right sides of the plume. The nomenclature of "left" and "right" sides corresponds to the perspective looking in the positive x-axis direction, i.e. in the flow direction. To rough description, the contour spacing is closer (i.e., steeper gradient) on the outside curvature of the meander, and the contour spacing is further apart (i.e., weaker gradient) on the inside curvature. Figure 9a displays the phase-averaged concentration profiles oriented perpendicular to the local plume centerline (y_0-direction) for the meandering plume for phase $\varphi = 0°$ at three downstream distances. In contrast to straight plume concentration profiles (Crimaldi et al. 2002; Rahman and Webster 2005; Crimaldi and Koseff 2006) and the meandering plume theory of Gifford (1959) and Sawford and Stapountzis (1986), the phase-averaged concentration profiles for the meandering plume are neither symmetric nor Gaussian in shape. Even at a comparatively short downstream distance ($x/UT = 0.47$) the profile is noticeably skewed, corroborating the asymmetric contour field observed in Fig. 8. As discussed relative to the field plot, the plume is consistently skewed with a weaker concentration gradient on the inside curvature side of the plume centerline.

For straight plumes, the concentration profiles are typically normalized by the centerline concentration and the plume width (as measured by the standard deviation of the concentration profile), then compared to determine self-similarity. The profiles shown in Fig. 9a are clearly not self-similar if the plume width is estimated using the standard deviation of the entire profile. However, the profiles can be divided into two parts—one to either side of the plume centerline—and the plume half-width can be determined for each side individually. If each side of the plume is normalized by its respective plume half-width (and the

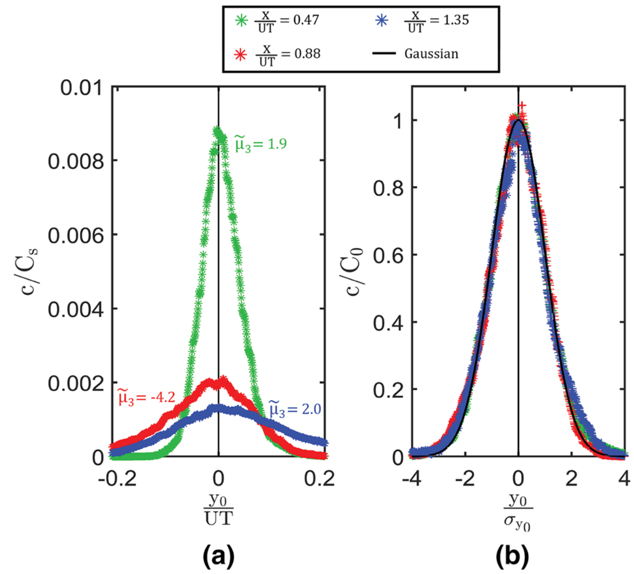

Fig. 9 Phase-averaged concentration profiles for the meandering plume for phase $\varphi = 0°$. **a** The phase-averaged concentration profiles normalized by the source concentration (c/C_S). **b** The phase-averaged concentration profiles normalized by the centerline concentration (c/C_0) versus the transverse coordinate normalized by the side-specific plume width ($\sigma_{y_0} = \sigma_L$ if $y_0 < 0$ and $\sigma_{y_0} = \sigma_R$ if $y_0 > 0$). $\tilde{\mu}_3$ is the normalized skewness parameter, which quantifies the asymmetry of the profile shape

concentration continues to be normalized by the centerline concentration), the profiles for the meandering plume are self-similar and Gaussian in a segmented sense, as shown in Fig. 9b.

The plume width for straight plumes is typically defined in terms of the standard deviation of the transverse concentration profiles (i.e., plume width $= 4\sigma$). As the meandering plumes are Gaussian in a segmented sense, it is more appropriate to define the plume width as $2(\sigma_L + \sigma_R)$, where σ_L and σ_R are the standard deviations of the left and right sides, respectively, of the concentration profile perpendicular to the local plume centerline. To examine its growth, the meandering plume width is plotted as a function of downstream distance in Fig. 10—along with the plume width of the straight plume for comparison. The meandering plume width increases more rapidly than the straight plume width. The plume width of an unconfined straight plume (with constant diffusion coefficient) grows as $x^{1/2}$ (e.g., Fischer et al. 1979; Roberts and Webster 2002). Straight plumes developing in a turbulent boundary layer grow more rapidly—the straight plume width observed in this study, and in Rahman and Webster (2005), grows as $x^{3/4}$. The same growth rate (i.e., as $x^{3/4}$) is also observed in slender plumes in uniformly sheared flow (Vanderwel and Tavoularis 2014a). As observed in Fig. 10, the plume width for the meandering plume developing in a turbulent boundary layer grows faster

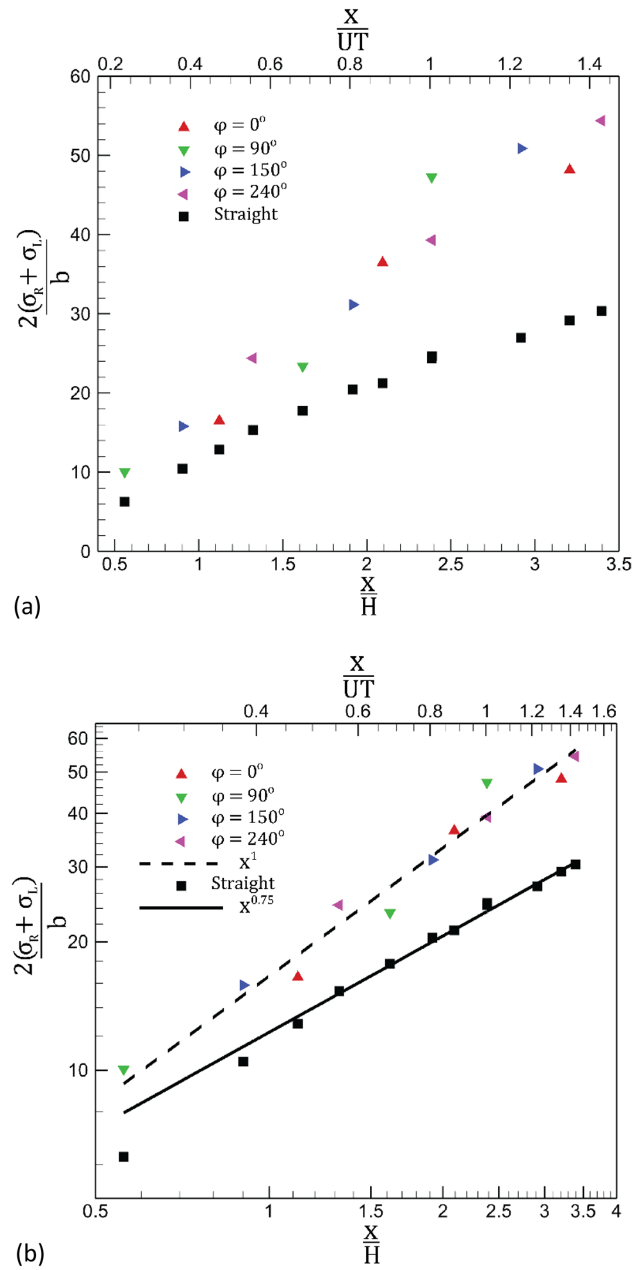

Fig. 10 The meandering plume width $\left[\frac{2(\sigma_L+\sigma_R)}{b}\right]$ and straight plume width $\left(\frac{4\sigma}{b}\right)$ as a function of downstream distance shown on **a** linear axes, and **b** logarithmic axes

still (as x^1), consistent across all four phases of the meandering plume. Fong and Stacey (2003) also reported the growth rate of plume width in a coastal meandering plume. The growth rate followed a scale-dependent dispersion law that was greater than the growth of the $x^{1/2}$ reference case, as well.

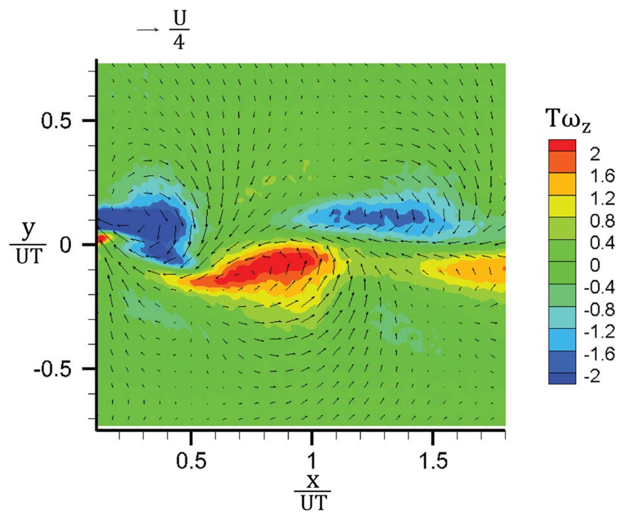

Fig. 11 Phase-averaged velocity (shown with vectors) and vorticity (shown with color contours) fields for the meandering plume for phase $\varphi = 0°$. The vectors shown are of the phase-averaged velocity with the free-stream velocity (U) subtracted. Every 5th velocity vector is plotted see Fig 13

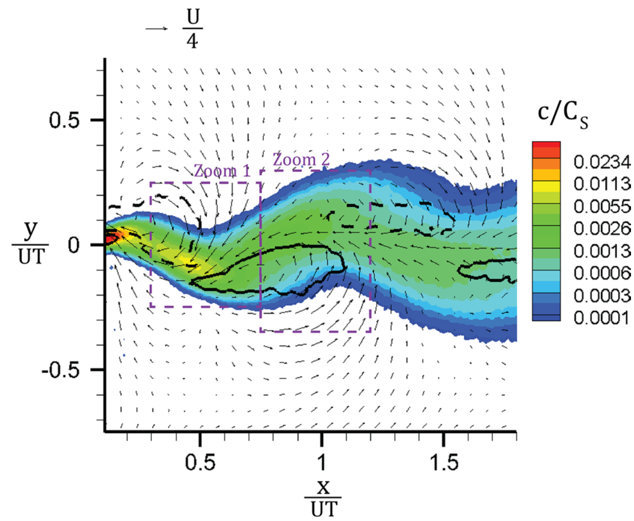

Fig. 12 Phase-averaged concentration field of the meandering plume for phase $\varphi = 0°$. Vorticity iso-contours corresponding to levels $T\omega_z = -1.3$ and $T\omega_z = 1.3$ are shown as dashed and solid black lines, respectively. The vectors indicate the phase-averaged velocity with the free-stream velocity (U) subtracted. Every 5th velocity vector is plotted. The purple boxes define the zoom regions (see Fig. 13)

3.5 Local peaks in the phase-averaged concentration

Figure 7a reveals local peaks in the phase-averaged concentration along the plume centerline. At first impression, this observation seems counterintuitive since one would not expect the centerline concentration to locally increase with downstream distance. The explanation comes by examining the large-scale alternating-sign vortices inducing the meander. To explore this, consider the phase-averaged vorticity field for the meandering plume for phase $\varphi = 0°$ shown in Fig. 11. The velocity vectors plotted in Fig. 11 are the phase-averaged velocity field with the free-stream velocity (U) subtracted, hence the velocity field in a frame of reference moving with the bulk flow. The large-scale alternating-sign vortices are easily identifiable in the phase-averaged vorticity field, and the velocity vectors show a clear rotational motion around the vortices in which the free-stream fluid is being swept into the plume by the large vortical motion.

To directly consider the effect these vortices have on the concentration field, Fig. 12 shows the phase-averaged concentration field of the meandering plume for phase $\varphi = 0°$. Figure 12 includes the phase-averaged velocity field with the free-stream velocity (U) subtracted, and the vorticity iso-contours corresponding to levels $T\omega_z = -1.3$ and $T\omega_z = 1.3$ to mark the position of the alternating-sign vortices. The vortex cores were also identified using the λ_2-criterion (Jeong and Hussain 1995). The iso-contours of vorticity are shown here since they identify the same region and are slightly smoother curves compared to the λ_2 iso-contours. Note that the local peaks in the phase-averaged concentration are located at the intersection of the counter-rotating vortices. Figure 13 shows two zoomed-in fields surrounding the local concentration peaks revealed in Fig. 12—referred to as "zoom 1" and "zoom 2", respectively. In these regions, the phased-averaged fluid motion in this frame of reference appears to be funneled between the counter-rotating vortices directly into the region of the local peak in phase-averaged concentration. Note that this does not physically correspond to a flow reversal, but rather to a local deceleration of the flow—as the free-stream velocity has been subtracted in this plot. The entrainment of fluid into the plume by this vortex-induced motion contributes to the increased "stirring" of scalar in the meandering plume, causing the concentration to decrease more rapidly with downstream distance than the straight plume (see Fig. 6b). However, the local deceleration effectively "piles up" the filaments of scalar that are advecting downstream, resulting in a local peak in the phase-averaged concentration in the space between the counter-rotating vortices. Vanderwel and Tavoularis (2016) reported a similar phenomenon at a smaller scale where hairpin turbulent vortices were responsible for strong scalar flux events and preferentially segregated the scalar quantity relative to the vortex structure.

Further evidence of this phenomenon is observed in the plots of the intermittency factor along the plume centerline shown in Fig. 14. The intermittency factor is defined as the percentage of time that the concentration at a specific location exceeds a threshold fraction of the source concentration (Chatwin and Sullivan 1989). A local peak in the intermittency factor co-located with the first peak in the

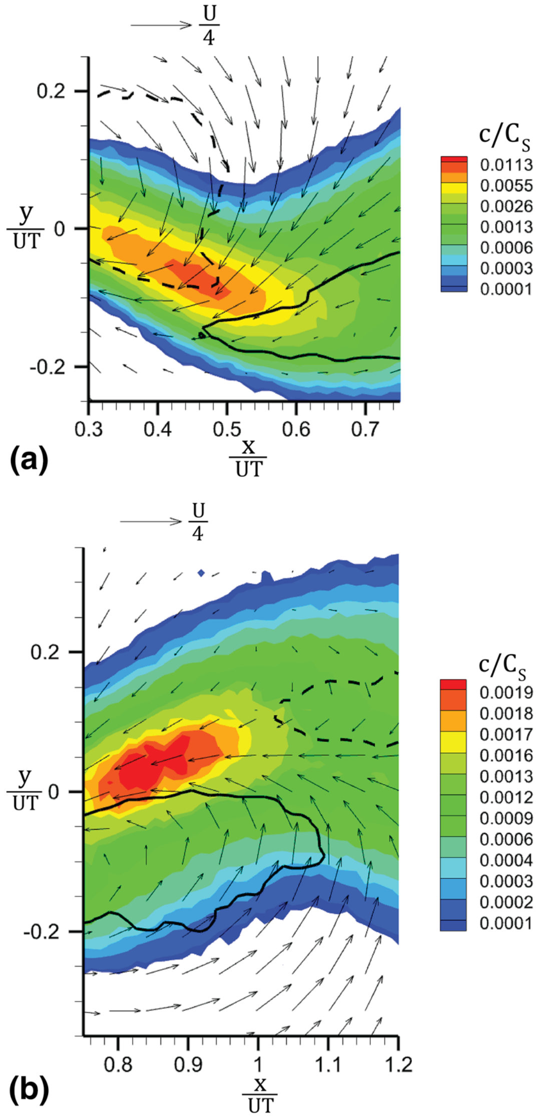

Fig. 13 Phase-averaged concentration field of the meandering plume for phase $\varphi = 0°$ shown for the **a** zoom 1 and **b** zoom 2 regions defined in Fig. 12. Vorticity iso-contours corresponding to levels $T\omega_z = -1.3$ and $T\omega_z = 1.3$ are shown as dashed and solid black lines, respectively. The vectors indicate the phase-averaged velocity with the free-stream velocity (U) subtracted. Every 4th velocity vector is plotted

phase-averaged concentration (at $x/UT \cong 0.45$) is observed for all of the chosen threshold concentrations (note that the choice of y-axis-range cuts off the intermittency factor profile for a threshold concentration of 1% of the source concentration). Further, local peaks in the intermittency factor are observed at threshold concentrations of 1% and 2% of the source concentration co-located with the second local peak in the phase-averaged concentration (at $x/UT \cong 0.85$). The intermittency has a local peak because filaments of high concentration are more likely to be observed in the region between the two vortices since they are "stalled" by the local deceleration in the phase-averaged flow field. The process is represented pictorially in Fig. 15. In this phenomenological model, fluid is drawn into the region between the alternating-sign large vortical structures, which has the effect of creating the general meandering shape of the plume. The induced motion also has the effect of aggregating high concentration filaments in the decelerated region between the vortices. As represented in the sketch, the net effect is to locally increase the intermittency and the phase-averaged concentration.

4 Conclusions

Examining the spatial interaction of the phase-averaged velocity field and phase-averaged concentration field in a meandering plume reveals the key influence of the

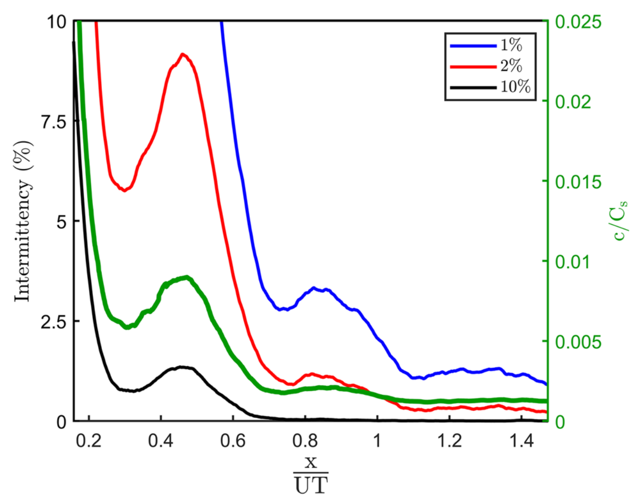

Fig. 14 Intermittency factor along the plume centerline for three thresholds (1%, 2%, and 10% of the plume source concentration, C_S) for the meandering plume for phase $\varphi = 0°$. The phase-averaged concentration along the centerline is shown in green

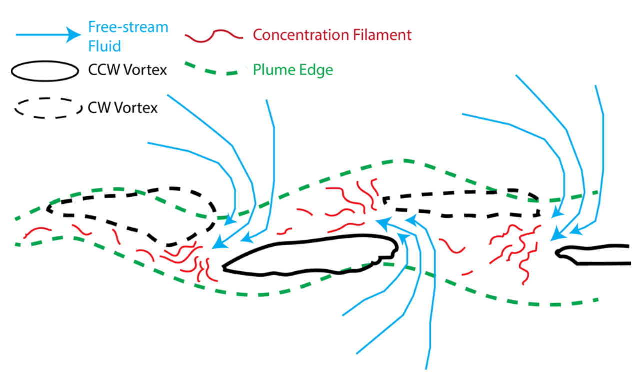

Fig. 15 Cartoon of the scalar filament transport by the large-scale alternating vortices

large-scale alternating-sign vortices on the transport of the scalar and the structure of the concentration distribution. By phase-locking the measurements, the turbulent processes may be examined separately from the effects of the large-scale vortical structures. Analysis of the phase-averaged concentration fields and transects perpendicular to the local plume centerline reveal that the symmetry about the plume centerline is broken due to the meandering. Nevertheless, phase-averaged concentration profiles are found to be Gaussian in a segmented sense for the meandering plume. Mixing and dilution is enhanced by the plume meander leading to a significantly reduced concentration along the plume centerline compared to a straight plume. Furthermore, the width of the meandering plume in a turbulent boundary layer grows more rapidly with downstream distance (as x^1) than the width of straight plumes (as $x^{3/4}$).

The large-scale alternating-sign vortices induce the plume meander, entrain free-stream fluid into the plume, and contribute to the more rapid dilution of scalar concentration in the meandering plume relative to the straight plume. The enhanced spread rate, dilution, and intermittency, as well as spatial and temporal variability of the field, may explain why aquatic organisms have significantly worse chemical plume tracking performance in a meandering plume (Page et al. 2011a,2011b). The large-scale alternating-sign vortices also cause local decelerations in the streamwise velocity along the plume centerline, which leads to localized aggregation of scalar filaments in the gap between the counter-rotating vortices. This aggregation of scalar filaments causes local peaks in the intermittency and phase-averaged concentration.

These results shed light on the structure of meandering plumes and provide guidance for field studies of larger-scale meandering plumes. In particular, the finding of a non-symmetric concentration profile is of significance to models of atmospheric meandering plumes, which often assume symmetry, and to studies of mixing in the wake of bluff bodies. Local peaks in the phase-averaged concentration are observed to be linked to the presence of the periodic large-scale alternating-sign vortices shed from the diverting plate, similar to the observations in the wake of a bluff body by Balu et al. (2001) and von Carmer et al. (2009). In Young et al. (2022), the turbulent flux of scalar for the meandering plume is related to more general turbulent mixing studies concerning the theory and application of the eddy diffusivity hypothesis.

Acknowledgements The authors gratefully acknowledge financial support provided by the University of Gothenburg, the Swedish Research Council FORMAS (Dnr: 2012-1134), and the U.S. National Science Foundation via Grant OCE-1234449. Additionally, the authors thank Dr. Phil Roberts (Georgia Institute of Technology) for helpful discussions.

References

Anfossi D, Oettl D, Degrazia G, Goulart A (2005) An analysis of sonic anemometer observations in low wind speed conditions. Bound-Layer Meteorol 114:179–203. https://doi.org/10.1007/s10546-004-1984-4

Arcoumanis C, McGuirk JJ, Palma JMLM (1990) On the use of fluorescent dyes for concentration measurements in water flows. Exp Fluids 10:177–180. https://doi.org/10.1007/BF00215028

Balu M, Balachandar R, Wood H (2001) Concentration estimation in two-dimensional bluff body wakes using image processing and neural networks. J Flow vis Image Process 8:121–139. https://doi.org/10.1615/JFlowVisImageProc.v8.i2-3.30

Bara BM, Wilson DJ, Zelt BW (1992) Concentration fluctuation profiles from a water channel simulation of a ground level release. Atmos Environ 26:1053–1062. https://doi.org/10.1016/0960-1686(92)90037-L

Bo JC, Hui DL, Fang LD (2003) Study of concentration fields in turbulent wake regions. J Hydraul Res 41:311–318. https://doi.org/10.1080/00221680309499975

Chatwin PC, Sullivan PJ (1989) The intermittency factor of scalars in turbulence. Phys Fluids A 1:761–763. https://doi.org/10.1063/1.857372

Cramp A, Coulson M, James A, Berry J (1991) A note on the observed and predicted flow patterns around islands—Flat Holm, the Bristol channel. Int J Remote Sens 12:1111–1118. https://doi.org/10.1080/01431169108929714

Crimaldi JP (2008) Planar laser induced fluorescence in aqueous flows. Exp Fluids 44:851–863. https://doi.org/10.1007/s00348-008-0496-2

Crimaldi JR, Koseff JR (2006) Structure of turbulent plumes from a momentumless source in a smooth bed. Environ Fluid Mech 6:573–592. https://doi.org/10.1007/s10652-006-9007-2

Crimaldi JP, Wiley MB, Koseff JR (2002) The relationship between mean and instantaneous structure in turbulent passive scalar plumes. J Turbul. https://doi.org/10.1088/1468-5248/3/1/014

Csanady GT (1973) Turbulent diffusion in the environment. D. Reidel Publishing Co., Boston

DeFelice TP, Meyer DJ, Xian G, Christopherson J, Cahalan R (2000) Landsat-7 reveals more than just surface features in remote areas of the globe. Bull Am Meteorol Soc 81:1047–1049. https://doi.org/10.1175/1520-0477(2000)081%3c1047:CAA%3e2.3.CO;2

Etling D (1990) On plume meandering under stable stratification. Atmos Environ 24:1979–1985. https://doi.org/10.1016/0960-1686(90)90232-C

Ferrier AJ, Funk DR, Roberts PJW (1993) Application of optical techniques to the study of plumes in stratified fluids. Dyn Atmos Oceans 20:155–183. https://doi.org/10.1016/0377-0265(93)90052-9

Fischer HB, List EJ, Koh RCY, Imberger J, Brooks NH (1979) Mixing in inland and coastal waters. Academic Press, New York

Fong DA, Stacey MT (2003) Horizontal dispersion of a near-bed coastal plume. J Fluid Mech 489:239–267. https://doi.org/10.1017/S002211200300510X

Franzese P (2003) Lagrangian stochastic modeling of a fluctuating plume in the convective boundary layer. Atmos Environ 37:1691–1701. https://doi.org/10.1016/S1352-2310(03)00003-7

Gifford F (1959) Statistical properties of a fluctuating plume dispersion model. Adv Geophys 6:117–136. https://doi.org/10.1016/S0065-2687(08)60099-0

Hanna SR (1984) Concentration fluctuations in a smoke plume. Atmos Environ 18:1091–1106. https://doi.org/10.1016/0004-6981(84)90141-0

Hanna SR (1986) Spectra of concentration fluctuations: the two time scales of a meandering plume. Atmos Environ 20:1131–1137. https://doi.org/10.1016/0004-6981(86)90145-9

Ingram RG, Chu VH (1987) Flow around islands in Rupert Bay: An investigation of the bottom friction effect. J Geophys Res Oceans 92:14521–14533. https://doi.org/10.1029/JC092iC13p14521

Jeong J, Hussain F (1995) On the identification of a vortex. J Fluid Mech 285:69–94. https://doi.org/10.1017/S0022112095000462

Kristensen L, Jensen NO, Petersen EL (1981) Lateral dispersion of pollutants in a very stable atmosphere—the effect of meandering. Atmos Environ 15:837–844. https://doi.org/10.1016/0004-6981(81)90288-2

Law AWK, Wang H (2000) Measurements of mixing processes using combined digital particle tracking velocimetry and planar laser induced fluorescence. Exp Therm Fluid Sci 22:213–229. https://doi.org/10.1016/S0894-1777(00)00029-7

Liao Q, Cowen EA (2010) Relative dispersion of a scalar plume in a turbulent boundary layer. J Fluid Mech 661:412–445. https://doi.org/10.1017/S0022112010003058

Luhar AK, Hibberd MF, Borgas MS (2000) A skewed meandering plume model for concentration statistics in the convective boundary layer. Atmos Environ 34:3599–3616. https://doi.org/10.1016/S1352-2310(00)00111-4

Marro M, Nironi C, Salizzoni P, Soulhac L (2015) Dispersion of a passive scalar fluctuating plume in a turbulent boundary layer. Part II: analytical modelling. Bound Layer Meteorol 156:447–469. https://doi.org/10.1007/s10546-015-0041-9

Mortarini L, Franzese R, Ferrero E (2009) A fluctuating plume model for concentration fluctuations in a plant canopy. Atmos Environ 43:921–927. https://doi.org/10.1016/j.atmosenv.2008.10.035

Nironi C, Salizzoni P, Marro M, Mejean P, Grosjean N, Soulhac L (2015) Dispersion of a passive scalar fluctuating plume in a turbulent boundary layer. Part I: velocity and concentration measurements. Bound Layer Meteorol 156:415–446. https://doi.org/10.1007/s10546-015-0040-x

Oettl D, Goulart A, Degrazia G, Anfossi D (2005) A new hypothesis on meandering atmospheric flows in low wind speed conditions. Atmos Environ 39:1739–1748. https://doi.org/10.1016/j.atmosenv.2004.11.034

Page JL, Dickman BD, Webster DR, Weissburg MJ (2011a) Getting ahead: context-dependent responses to odorant filaments drive along-stream progress during odor tracking in blue crabs. J Exp Biol 214:1498–1512. https://doi.org/10.1242/jeb.049312

Page JL, Dickman BD, Webster DR, Weissburg MJ (2011b) Staying the course: chemical signal spatial properties and concentration mediate cross-stream motion in turbulent plumes. J Exp Biol 214:1513–1522. https://doi.org/10.1242/jeb.049304

Rahman S, Webster DR (2005) The effect of bed roughness on scalar fluctuations in turbulent boundary layers. Exp Fluids 38:372–384. https://doi.org/10.1007/s00348-004-0919-7

Reynolds AM (2000) Representation of internal plume structure in Gifford's meandering plume model. Atmos Environ 34:2539–2545. https://doi.org/10.1016/S1352-2310(99)00506-3

Ride DJ (1988) A model for the observed intermittency of a meandering plume. J Hazard Mater 19:131–137. https://doi.org/10.1016/0304-3894(88)85044-1

Roberts PJ, Webster DR (2002) Turbulent diffusion. In: Shen HH, Cheng AHD, Wang K, Teng MH, Liu CCK (eds) Environmental fluid mechanics: theories and applications. American Society of Civil Engineers, Reston, pp 7–47. https://doi.org/10.1002/9780470057339.vat029

Sawford BL, Stapountzis H (1986) Concentration fluctuations according to fluctuating plume models in one and two dimensions. Bound Layer Meteorol 37:89–105. https://doi.org/10.1007/BF00122758

Stacey MT, Cowen EA, Powell TM, Dobbins E, Monismith SG, Koseff JR (2000) Plume dispersion in a stratified, near-coastal flow: measurements and modeling. Cont Shelf Res 20:637–663. https://doi.org/10.1016/S0278-4343(99)00061-8

Sykes RI (1984) The variance in time-averaged samples from an intermittent plume. Atmos Environ 18:121–123. https://doi.org/10.1016/0004-6981(84)90234-8

Talluru KM, Philip J, Chauhan KA (2018) Local transport of passive scalar released from a point source in a turbulent boundary layer. J Fluid Mech 846:292–317. https://doi.org/10.1017/jfm.2018.280

Thomson RE, Gower JFR, Bowker NW (1977) Vortex streets in the wake of the Aleutian Islands. Mon Weather Rev 105:873–884. https://doi.org/10.1175/1520-0493(1977)105%3c0873:VSITWO%3e2.0.CO;2

Tracy HJ, Lester CM (1961) Resistance coefficients and velocity distribution smooth rectangular channel. US Geological Survey Water Supply Paper 1592-A. https://doi.org/10.3133/wsp1592A

Van Dyke M (1982) An album of fluid motion. Parabolic Press, Stanford

Vanderwel C, Tavoularis S (2014a) Measurements of turbulent diffusion in uniformly sheared flow. J Fluid Mech 754:488–514. https://doi.org/10.1017/jfm.2014.406

Vanderwel C, Tavoularis S (2014b) Relative dispersion of a passive scalar plume in turbulent shear flow. Phys Rev E 89:041005(R). https://doi.org/10.1103/PhysRevE.89.041005

Vanderwel C, Tavoularis S (2016) Scalar dispersion by coherent structures in uniformly sheared flow generated in a water tunnel. J Turbul 17:633–650. https://doi.org/10.1080/14685248.2016.1155713

von Carmer CF, Rummel AC, Jirka GH (2009) Mass transport in shallow turbulent wake flow by planar concentration analysis technique. J Hydraul Eng 135:257–270. https://doi.org/10.1061/(ASCE)0733-9429(2009)135:4(257)

Webster DR, Rahman S, Dasi LP (2003) Laser-induced fluorescence measurements of a turbulent plume. J Eng Mech 129:1130–1137. https://doi.org/10.1061/(ASCE)0733-9399(2003)129:10(1130)

Webster DR, Roberts PJW, Ra'ad L (2001) Simultaneous DPTV/PLIF measurements of a turbulent jet. Exp Fluids 30:65–72. https://doi.org/10.1007/s003480000137

Wilson DJ, Robins AG, Fackrell JE (1985) Intermittency and conditionally-averaged concentration fluctuation statistics in plumes. Atmos Environ 19:1053–1064. https://doi.org/10.1016/0004-6981(85)90189-1

Wolanski E, Imberger J, Heron ML (1984) Island wakes in shallow coastal waters. J Geophys Res Oceans 89:10553–10569. https://doi.org/10.1029/JC089iC06p10553

Yee E, Wilson DJ (2000) A comparison of the detailed structure in dispersing tracer plumes measured in grid-generated turbulence with a meandering plume model incorporating internal fluctuations. Bound Layer Meteorol 94:253–296. https://doi.org/10.1023/A:1002457317568

Yee E, Chan R, Kosteniuk PR, Chandler GM, Biltoft CA, Bowers JF (1994) Experimental measurements of concentration fluctuations and scales in a dispersing plume in the atmospheric surface layer obtained using a very fast response concentration detector. J Appl Meteorol 33:996–1016. https://doi.org/10.1175/1520-0450(1994)033%3c0996:EMOCFA%3e2.0.CO;2

Young DL, Webster DR, Larsson AI (2022) Structure and mixing of a meandering turbulent chemical plume. Turbulent mixing and eddy-diffusivity. Submitted.